BOLETIN DE LA SOCIEDAD ESPAÑOLA DE
Cerámica y Vidrio
www.elsevier.es/bsecv

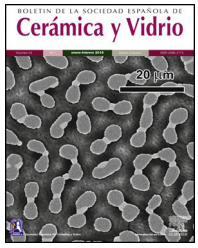

Interaction at high temperature of Popocatépetl volcanic ash deposited on yttria-stabilized zirconia sintered coupons

Fernando Juárez López[a,*], *Diana Monserrat Vivian Sánchez*[b], *Jose C. Jiménez Escalona*[b], *Rubén Cuamatzi Meléndez*[a], *Ángel de Jesús Morales Ramirez*[c], *Margarita García Hernández*[d]

[a] *Instituto Politécnico Nacional, CIITEC, Cerrada de Cecati, Sta. Catarina, 02250 Ciudad de México, Mexico*
[b] *Instituto Politécnico Nacional-ESIME Ticoman, Av. Ticomán No. 600, Col. San José Ticomán, Gustavo A. Madero, 07340 Ciudad de México, Mexico*
[c] *Instituto Politécnico Nacional, ESIQIE, UPAL Zacatenco, Av Luis Enrique Erro, 07730 Ciudad de México, Mexico*
[d] *Instituto Politécnico Nacional – UPIIH, Carretera Pachuca Actopan Km 1+500, Distrito de Educación, Salud, Ciencia, Tecnología e Innovación, 42162 San Agustín Tlaxiaca, Hidalgo, Mexico*

ARTICLE INFO

Article history:
Received 19 June 2024
Accepted 27 January 2025
Available online 27 February 2025

Keywords:
7YSZ
Melted ash
Sintering
Degradation

ABSTRACT

This work aims to study the interaction of sintered yttria-stabilized zirconia (7YSZ) ceramic under a volcanic ash mix at an engine representative temperature of 1350 °C. In this work, two different locations – distance from Mexico Popocatépetl Volcano were chosen to collect the ashes, and to perform their melting process with variable chemical composition. Afterward, each ash was deposited on the surface of 7YSZ ceramic coupons, then they were exposed at heating and cooling cycles at designed temperature equal to 1350 °C. After 8 cycles of thermal treatment testing of 8 h, the morphology and microstructure analysis of the 7YSZ coupons was carried out using microscopy and X-ray diffraction analysis techniques. The results showed that a molten ash layer, with smooth morphology of size of 60 μm of thick, was formed on the ceramic surface. Based on the observed degradation, the general status of the coupons after 8 cycles of thermal test, presented failure by growth of large cracks which were associated to the infiltration of melted ash through the thickness of ceramic coupon. This melted ash infiltrated trough the fine grain microstructure, promoted the development of a compose rich in silica, which is brittle and therefore promoted cracks initiation with subsequent propagation in the substrate.

* *Corresponding author.*
E-mail address: fjuarezl@ipn.mx (F. Juárez López).
https://doi.org/10.1016/j.bsecv.2025.01.002

Interacción a alta temperatura de ceniza volcánica del Popocatépetl depositada sobre pastillas sinterizadas de circonia estabilizada con itria

Palabras clave:
7YSZ
Ceniza fundida
Sinterización
Degradación

RESUMEN

Este trabajo tiene como objetivo estudiar la interacción de cerámica de circonia estabilizada con itria (7YSZ) sinterizada, bajo una mezcla de ceniza volcánica a una temperatura representativa de operación de 1350 °C. En este trabajo, se eligieron dos ubicaciones diferentes y cercanas del volcán Popocatépetl de México, para recolectar las cenizas, y caracterizar su proceso de fusión de composición química variable. Posteriormente, estas cenizas se depositaron sobre la superficie de pastillas cerámicas de 7YSZ, y se expusieron a ciclos de calentamiento a una temperatura de 1350 °C, y lento enfriamiento a temperatura ambiente. Después de 8 ciclos térmicos de 8 horas, un análisis de morfología y microestructura de las pastillas cerámicas se llevó a cabo mediante técnicas de microscopía y difracción de rayos X. Como resultado, una capa vítrea de cenizas fue formada sobre la superficie de las pastillas cerámicas, con morfología suave de tamaño de 60 μm de espesor. Con base en la degradación observada, el estado general de la pastilla cerámica luego de 8 ciclos térmicos presentó falla por crecimiento de grandes grietas, las cuales estuvieron asociadas a la infiltración de cenizas fundidas a través del espesor de la pastilla cerámica. La ceniza fundida infiltró a través de la microestructura de grano fino promoviendo el desarrollo de un compuesto rico en sílice, el cual tiene características frágiles y por lo tanto promovió la iniciación de grietas con la subsecuente propagación en el substrato.

Introduction

Environmental rubbles such as sand, dust and volcanic ash are considered as one of the major menaces for aeronautic turbines safety. Jet engines are inherently vulnerable to contamination which can cause unsafe and/or deficient operation [1–7]. The enter of volcanic ash in turbines aircrafts is broadly documented as a possible hazard in the aeronautic industry. Throughout the service operation of gas turbines along the time, the ingestion of volcanic ash can impact, melt, and adhere to thermal barrier coatings (TBCs) which protect hot-section parts, affecting their structural integrity, leading their aircraft instability. Accordingly, it is relevant to investigate the behaviour of volcanic ashes on jet engine components. Nowadays, several works have been developed to study the interaction of ash with ceramic materials, nonetheless in much research work, it was employed synthetic ash [4,5,8,9].

At high temperatures, molten ash can penetrate inside of the TBCs coating through porosity and/or cracks, with a rapid solidifying in the course of the cooling process. This reduces the strain tolerance of the coating, making the TBCs more prone to delamination during the thermal cycles [10–13]. Additionally, the permeable ash can react with the stabilizer in the coating to absorb Y^{3+} and Zr^{4+}, leading to the re-precipitation of Y-depleted. And this depletion can cause phase transition of ZrO_2 from t′-ZrO_2 to unstable monoclinic phase (m′-phase). Thus, volume expansion that accompanies the phase transformation, causes internal stress in the coating, inducing cracking into the coating [14–18]. In the literature, several studies have shown that the damage by synthetic ash to TBCs can be effectively reduced by promoting ash crystallization in order to suppress melt penetration into the coating [19–22]. Therefore, it can be observed that the interaction between different coating materials, and synthetic ash has been demonstrated to react strongly with synthetic ash, forming a dense reaction layer [23,24].

Nevertheless, volcanic ash, even with lower Silica content, has Y^{3+} solubility, revealing that more top-coat has to be consumed, to saturate the melted ash, and the chemical reaction is delayed and melted ash has more time to infiltrate. While nature volcanic ash has a relative high viscosity, exhibiting a large infiltration depth, the apatite compound with a theoretical $CaAl_x(SiO_y)_z$ structure, is the main corrosive product for either nature volcanic ash as synthetic ash [8–13]. This in turn, promotes the development of corrosion by precipitation of high-entropy apatite phases, causing the damage of the TBC's. However, the volcanic ash composition can improve the density and stability of the slow-growing reaction layer, hindering the further penetration of molten ash. Moreover, at high temperatures (around 1350 °C), a reaction layer with a three-layered morphology, ash has been reported [10], as resulting from the decreased viscosity of molten synthetic.

Recently, it was observed that the identification and distinguishing of self-crystallization and reactive crystallization of synthetic ash, become a significant subject for elucidating the interactions between coating materials and synthetic ash, and accordingly it can be used to develop new coating material systems against corrosive ash [1–5,12,13,23,24].

Hence, in this work it was designed an experimentally procedure that replicates the thermal conditions of nature volcanic ash effect on airplanes jet engines when travelling in

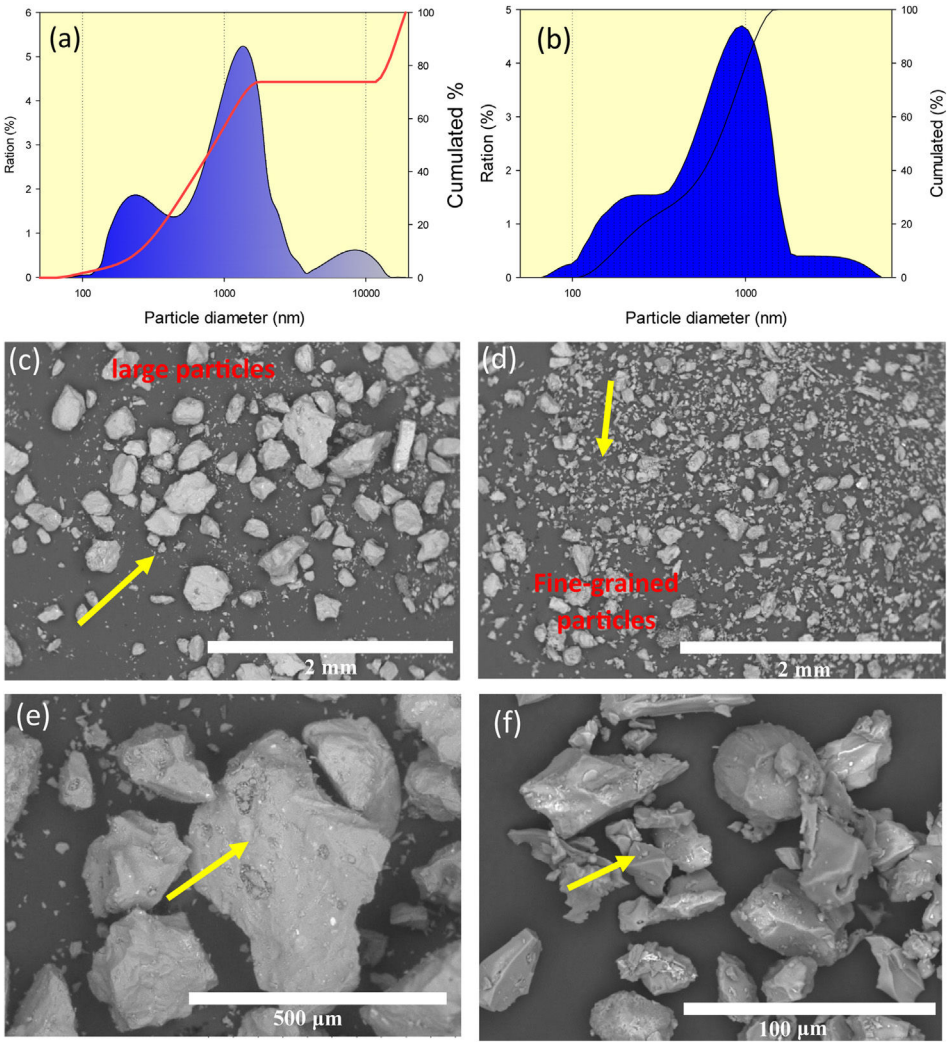

Fig. 1 – SEM micrographs analysis of volcanic ash obtained to land distance from Volcano: size distribution graphics of "A"and"B" ashes respectively, (c)(e)"A" and (d)(f) "B" respectively.

volcanic ash environments. Thus, the proposed work methodology shows the chemical interaction of nature volcanic ash in a ceramic material, this under a defined thermal treatment condition. In the work, it was employed Mexico Popocatepetl Volcanic ash deposited on 7YSZ ceramics materials components. The Popocatepetl ash was collected from two different land localizations with respect to the Volcano crater, this in order to study their effect behaviour, since it was identified that the chemical composition varies with the location where the ash is collected. Therefore, in the present work thermochemical reactions were caused by the ashes, at high temperature, in order to determinate the potential damage in 7YSZ ceramics samples, previously sintered by a sintering process. The results also showed that the present work is the first approach in the fields of volcanology and aviation, reported in the literature, and that allows the quantification of the interaction of the melting process of Mexican Popocatepetl ash with sintered 7YSZ ceramics.

Materials and methods

Popocatepetl Volcano ashes, from the months of March 2023 through April 2023 eruptions, were recollected from two land distance, with respect to Volcano crater, at 7 km and 25 km (hence A and B km as-collected). The ashes were characterized in order to determinate their chemical composition, size and morphology. 7YSZ ceramic cylindric coupons, with a diameter of 2 cm and a thickness of 3 mm were used as substrate to deposit the ashes. The ceramic coupons were obtained following a procedure descripted in previous own work [25]. The degradation corrosive environment, thermal treatments at a temperature of 1350 °C in atmospheric air, was carried out following similar procedure reported in the literature of deposit molten salts [26–28]: an ash ratio in the range of 20 mg/cm^2 was homogeneously deposited on each ceramic substrate, later the ash-coupon ensemble was then placed in an electric furnace at the ambient temperature.

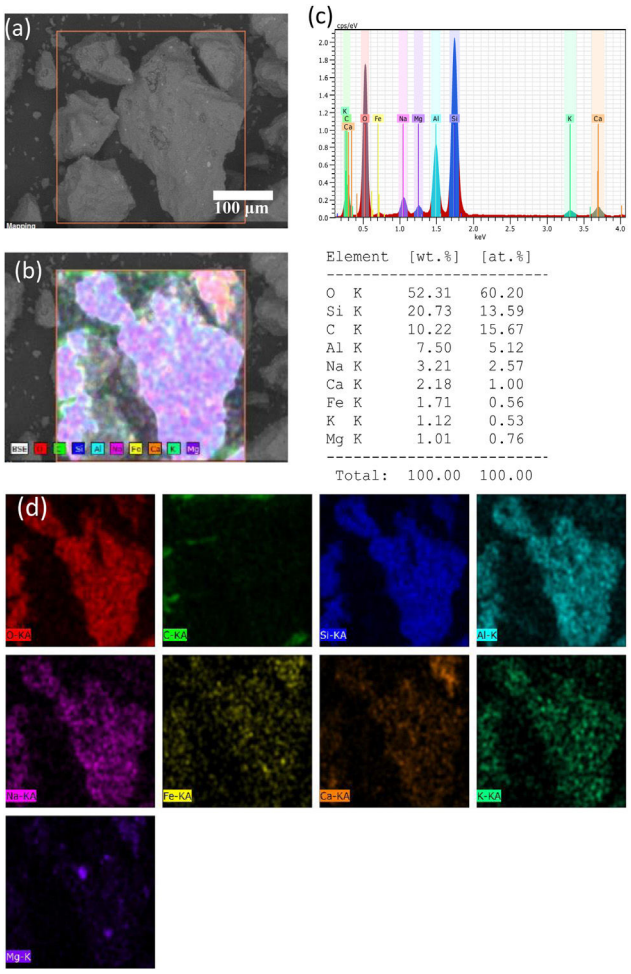

Fig. 2 – Images of "A" volcanic ash obtained to distance of 7 km from Volcano: (a) SEM micrograph analysis, (b) spectrum EDS analysis, and (c and d) mapping and spectrum EDS analysis respectively.

Afterward, a temperature ramp of 100 °C/min was imposed to furnace until the designed temperature of 1350 °C. Then, at the end of 8 h of staying at 1350 °C, the ash-coupon ensemble was cooled down inside the furnace at ambient temperature. And in turn each ash-coupon ensemble was visually inspected with the aim to identify the cracks appearance, and the cyclic thermal was repeated until the ash-ceramic coupon ensemble suffers catastrophic fail. Once the high-temperature treatment was performed, morphologic and microstructural analyses of the ash-coupon ensemble were carried out with a high-resolution scanning electron microscope (model JEOL-7800) with XL-EDAX Ametek-Apolo detector, Word Distance 10–12 mm and windows 30 mm, and 10–15 kV of accelerated energy. And an X-ray diffractometer X'PertPro (Bruker D8-ECO Advance) were also performed, with a Bragg-Brentano set-up, equipped with an X'Celeratrimina, in the range 20–80° (2 theta), using a 0.021 step size, 2 s time per step and Cu–Ka radiation of 1.541. A DSC instrument (SDT Q600 V20.9 Build 20) with module DSC-TGA Standard, Serial, 0600-0854, was used firstly at a ramp 50.00 °C/min to 600.00 °C temperature, second ramp of 10.00 °C/min to reach 1500.00 °C, this with the aim to assess transition phases of both ashes (as-collected at different distance from the Volcano).

Results and discussion

Popocatepetl Volcano ash characteristic

Fig. 1(a) and (b) shows the size distribution graphics of A and B ashes respectively. Hence, it is observed binomial features that would correspond to the presence of smalls and large particles for both ash cases. Moreover, micrographs of scanning electron microscopy micrographs showed the features of both volcanic ashes collected at different distance from the Volcano, Fig. 1(c)(d) A and (e)(f) B respectively.

From the figures, it is observed that "A" ash is composed by large particles in the size range from 100 to 400 μm, and with presence of a fine-grained fraction less than 10 μm, showing textural surface with a roughness feature and a granular morphology. In the case of "B" ash, it is observed than that is composed by a smoother fraction in the size range from 20 to 100 μm with porous morphology, and a fine-grained fraction less than 10 μm. An EDAX analysis is shown in Fig. 2, for the raw "A" volcanic ash (obtained at a distance of 7 km from Popocatépetl Volcano), it is shown a chemical composition composed by O, Si, C, Al, Na elements principally,

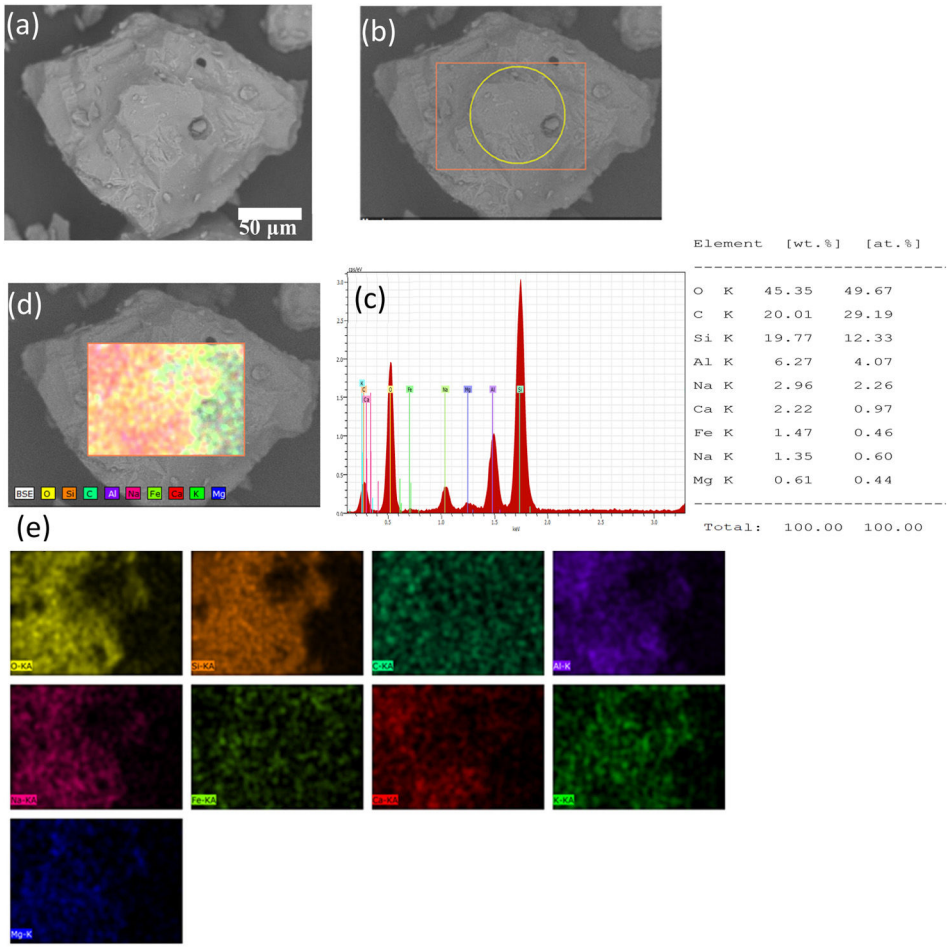

Fig. 3 – Images of "B" volcanic ash obtained to the distance of 25 km from Volcano: (a) SEM analysis, (b and c) EDS spectrum and quantitative analysis respectively, and (d and e) mapping and spectrum EDS analysis respectively.

and with minor content of Ca, Fe, K, and Mg chemical elements.

In the case of raw "B" volcanic ash, shown in Fig. 3, the EDAX analysis of volcanic ash (obtained to distance of 25 km from Popocatépetl Volcano), is composed by silica with a highest weight content of 12.33 wt.%, with an apparency of black color, this volcanic ash can be classified as a scoria based on the amount of silica [10,11].

The crystal structure of the ash particles was analyzed by XRD analysis. Fig. 4(a) shows the XRD analysis of the "A" ashes obtained at 7 km of distance from Volcano. In the figure it can be observed that the raw volcanic ash presented slight amount of an amorphous glass phase, estimated based on the broad range of $2\theta = 20°–37°$, with significant characteristic peaks of crystalline phases.

These last peaks can be attributed to the presence of $Al_{1.77}Ca_{0.88}O_8Si_{2.23}$_00-052-1344, and $Al_3Ca_2H_2Mg_4NaO_{24}Si_6$_00-023-1406. Both ashes, also presented crystal phases called plagioclase such as albite $Al_2CaO_8Si_2$_00-012-0301 and anorthite $AlNaO_8Si_3$_01-083-1606 [13,29–31]. Fig. 4(b) shows the XRD analysis of the "B" ashes obtained at 25 km of distance from Volcano, this raw volcanic ash also presented a slight amount of an amorphous glass phase, estimated based on the range theta $2\theta = 20°–37°$ with significant characteristic peaks of crystalline phases. These last peaks could be attributed to the presence of iron oxide phase such as magnetite $Fe_{2.937}O_4$ 01-086-1350 [32]. The DSC analysis is shown in Fig. 5(a) and (b) for both "A" and "B" ashes obtained from Volcano.

In summary, this DSC analysis leads to identify the decomposition, phase transition, oxidation, surface modification, or the withdrawal of volatile fraction solid from minerals and other materials, applied a thermal treatment. Both TGA-DSC curves, which were carried out in static air, with a heating rate of 10 °C/min at the ending, showed almost a thermal stable behaviour up to 1300 °C, with a weight loss in the range of 1.5–5%. Fig. 5(a) shows the TGA-DSC curve of "A" raw volcanic ash, which was performed using at the beginning a heating rate of 50 °C/min. As shown by the TGA curve, the "A" raw volcanic ash is almost thermally stable up to 1300 °C, with a small reduction in weight of about 5%. This weight loss could be attributed to the trapped gases, and that were released from ash particles during thermal heating. However, the DSC analysis ash appeared to be not thermally stable up to 550 °C. There is a very strong endothermic peak at around 700 °C, with an onset temperature of 820 °C, afterward it is showed a slight exothermic peak at around 950 °C, this can be due to calcination phenomenon of some ash component.

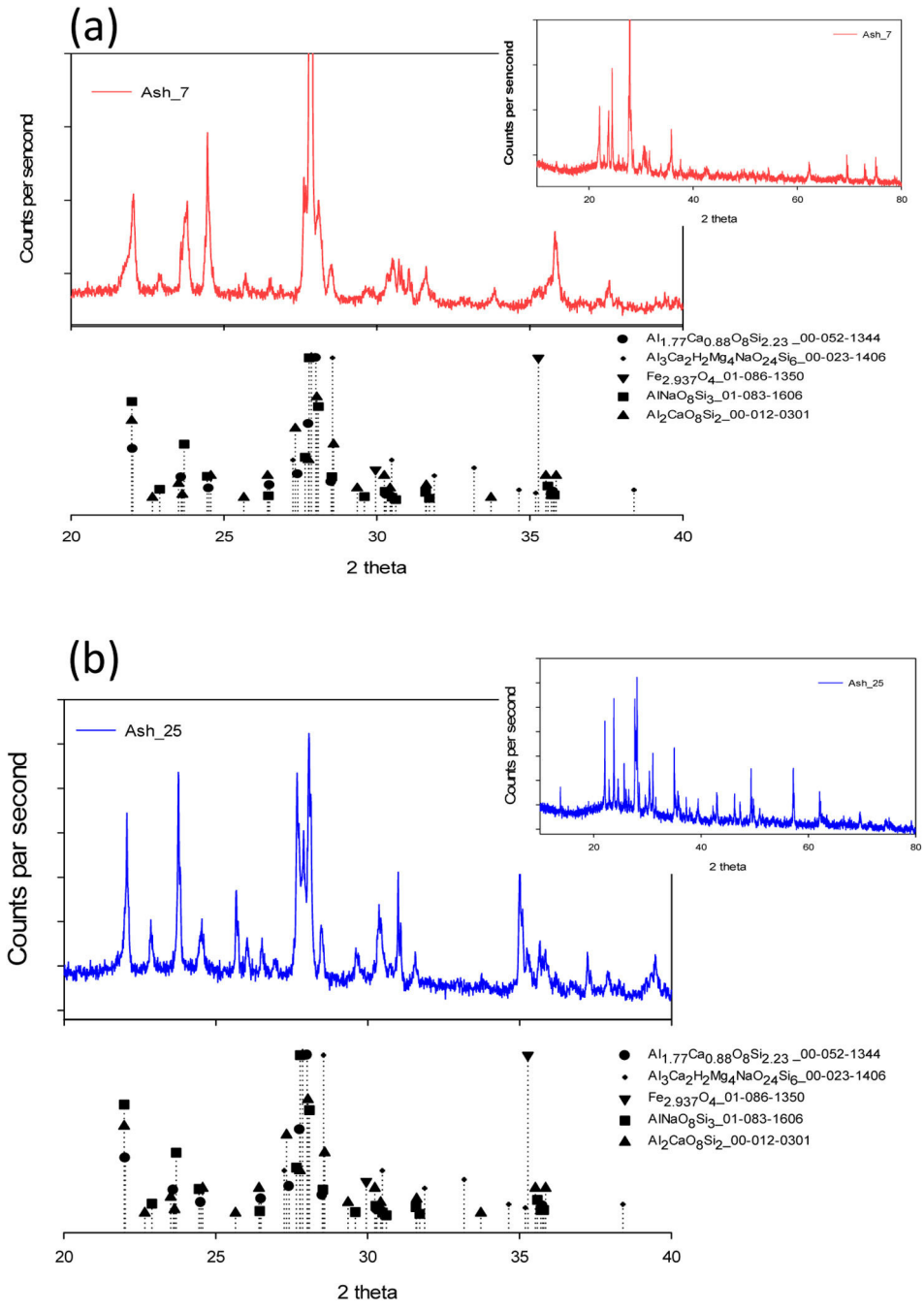

Fig. 4 – XRD analysis (a) "A" and (b) "B" of the ashes obtained from Volcano.

At the ending curve a strong endothermal peak at 1300 °C was associated to the melting point of raw volcanic ash. In the case of the "B" raw volcanic ash collected at 25 km from Volcano the TGA-DSC is shown in Fig. 5(b). The DSC curve exhibited a slight peak up to 550 °C, indicating that there is transformation at this low temperature. In addition, above 900 °C, a slight exothermic peak was exposed which can be attributed to an oxidation phenomenon [13]. This "B" raw volcanic ash is also thermally stable up to 1300 °C, with a reduction in weight of about 1.5%. This weight loss could be associated to a reduction phenomenon. Similarly, the DSC line showed a strong endothermal peak at a temperature of 1300 °C at the ending of the curve, which was related to vitrification process with fusion and structural changing of the mineral composition [10,11]. Therefore, the mineral composition, obtained with XRD for raw ash, can be associated to the transformation of one mineral phase, which can form a solid solution [13,32,33]. Nonetheless, these strong endothermic peaks could be related to the formation of a solid solution of magnetite. In accordance with the thermal analysis results, the two raw ashes samples were then thermally characterized up a temperature of 1350 °C in static air. Hence, it is expected that the ash particles melted to molten ashes, which was studied in the following sections of the

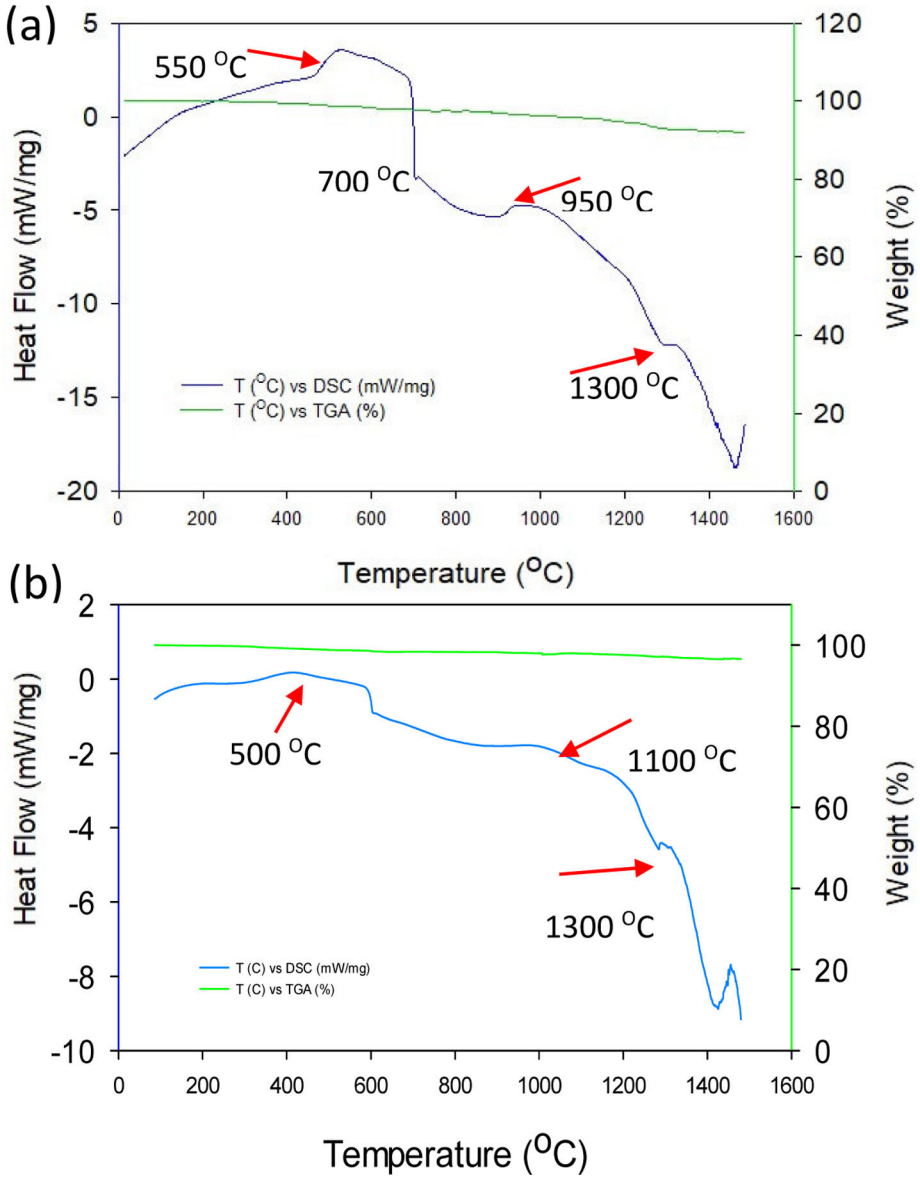

Fig. 5 – DSC analysis of the ashes collected: (a) "A" and (b) "B".

present work by XRD and SEM analyses, resulted from the interaction with ceramics materials prepared by a sintering process.

Thermal interaction ash versus 7YSZ ceramic

Fig. 6(a) shows a 7YSZ ceramic coupon, which was previously prepared by spark plasma sintering process, with diameter of 2 cm and thickness of 3 mm [25].

Fig. 6(b) shows the XRD analysis which corresponds well to ZrO_2 tetragonal structure, with indexed JCPDS 01-082-1241 pattern. Fig. 6(c) shows the microstructure of the 7YSZ ceramic coupon, which is composed by a morphology of grain size of around 3 μm. It is worth to note the presence of quite null porosity in the 7YSZ coupon. Furthermore, this low porosity can be associated to a low diffusion of melted ash into the 7YSZ matrix.

Upon ashes characterization, both "A" and "B" ash particles were homogeny distributed on ceramic surface, as depicted in Fig. 7(a). It is showed each ash deposit on 7YSZ coupons respectively before the thermal treatment at a temperature of 1350 °C. Then, after four thermal treatment cycles, images of both 7YSZ ceramic coupons, with melted "A" and "B" ashes, are observed in Fig. 7(b) and (c). Hence, "A" and "B" coupons respectively, it was not significant changes identified on the ceramic coupon surface at the end 4 cycles after thermal treatment at 1350 °C. Thus, ash vitrification was remained as shown by the images. It is clear that the color of ceramic substrate surfaces changed completely, which indicates the chemical reaction of the ashes. It was also observed that in "A" ceramic substrate surface coupon it was formed a thin layer of appearance vitrified with yellow coloration. A similar observation is shown for "B" ceramic substrate coupon, where the melted ash formed a layer with

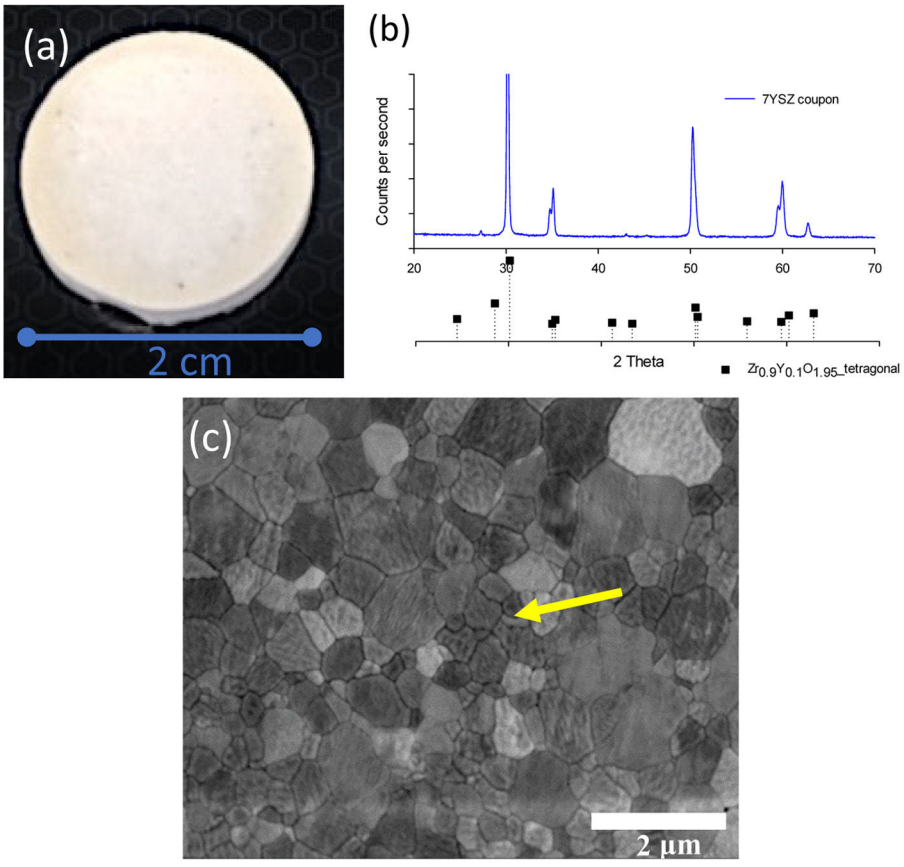

Fig. 6 – SEM analysis of 7YSZ ceramic before deposits of ashes: (a) coupon of diameter of 2 cm, (b) XRD analysis and (c) microstructure and morphology of grain.

appearance vitrified, but with a poor red coloration, as observed in Fig. 7(c). After thermal treatment at 1350 °C and 8 temperature cycles, the dimensions of the ceramics were not preserved in both "A" and "B" coupons (melted ash-7YSZ ceramic substrate) as clearly observed in Fig. 7(d) and (f). Here, the creation of large number of smalls microcracks were observed promoted the failure of the ceramic substrate, as clearly observed in both "A" and "B" surface coupons, where it was also observed the separation of the coupons. The XRD analysis of both cases study, after treatment at 1350 °C and 8 cycles with volcanic ash, are shown in Fig. 8(a) "A" coupon and (b) "B" coupon, respectively. This XRD analysis indicates the existing of decreased peaks in intensity, which were smoother compared to those of the raw ash sample. Fig. 8(a) shows the XRD experimental pattern of "A" ceramic coupon, in which a slight formation of amorphs phases can be identified and contributing to the indexed patterns. This indexed patterns also included $Al_{1.77}Ca_{0.88}O_8Si_{2.23}$ 00-052-1344 and $Al_3Ca_2H_2Mg_4NaO_{24}Si_6$ 00-023-1406 structure and a crystalline phase majority composed by $Zr_{0.9}Y_{0.1}O_{1.95}$ tetragonal 01-082-1241, and minor composed by ZrO_2 monoclinic phase 23-002-96 respectively, as it was determined by quantitative Rietveld analysis. This last result means the presence of a transition of 7YSZ tetragonal phase to ZrO_2 monoclinic during thermal treatment, which it could be due to the depletion of Y by reaction with melted ashes constituents. This Y depletion has been reported in 7YSZ by different authors including own works [26–28].

In the same sense, after thermal treatment test at 1350 °C, of "B" coupon, it can be observed from Fig. 8(b) that a major amorph phase, and a slight crystalline phase were presented. These, new crystallizing phases appeared, such as magnetite $Fe_{2.937}O_4$ or pargasite ($NaCa_2Mg_4Al_3Si_6O_{24}(OH)_2$), which can be correlated with a change in color from black to poor red, above exposed. These changes have been attributed to the recrystallization of the minerals, oxidation of magnetite or other iron oxides, or/and transformation into hematite, which has a red silica color, as also found in the literature [11,12]. SEM analysis of the "A" coupons after 4 cycles thermal treatment at 1350 °C is shown in Fig. 9.

It was observed the formation of microcracks in the range size from 1.5 to 2.0 mm, along with a few isolated pores, in Fig. 9(a) and (b). A close-up view on the sample, clearly shows the morphology spheric of these pores, as observed in Fig. 9(c). Thus, the melted ash initially formed a thick dense vitrified layer that interacted with the 7YSZ ceramic surface by the possible formation of a semi-continuous silica thin film, shaped at the interface with the substrate at 1350 °C. Similarly, the SEM analysis of the "B" coupon after 4 cycles thermal treatment at 1350 °C with B volcanic ash is shown in Fig. 10.

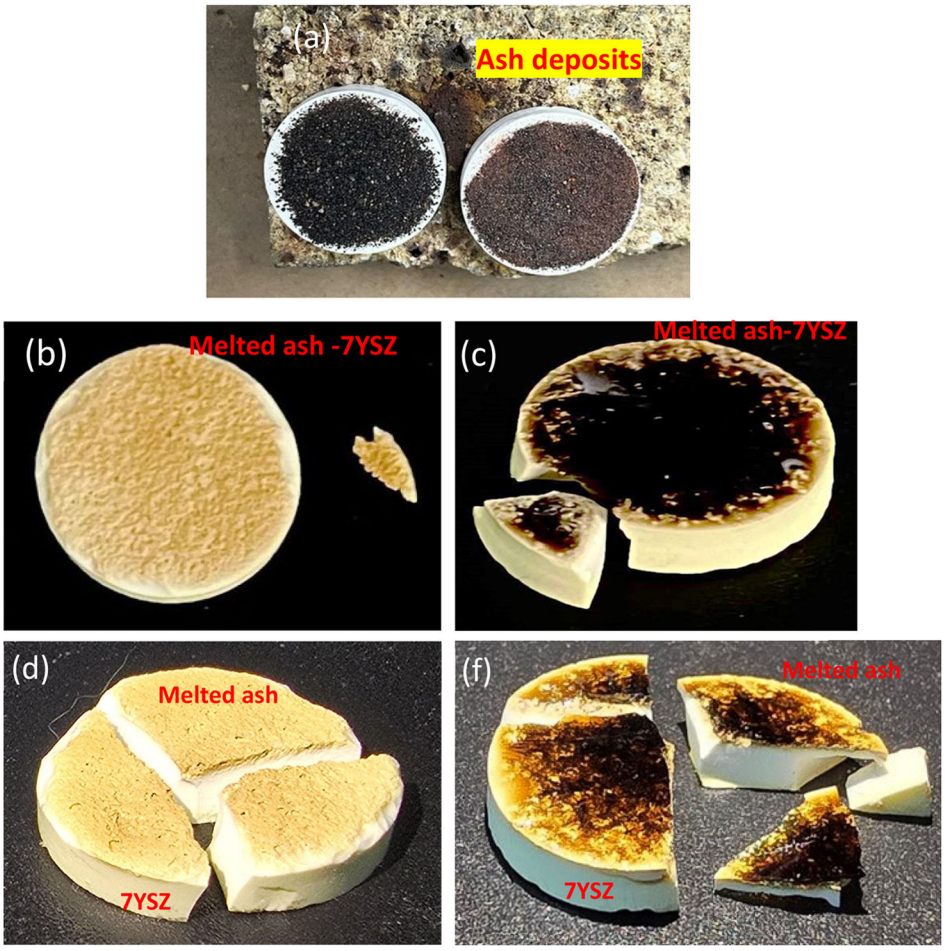

Fig. 7 – Images of 7YSZ ceramics with deposit of ashes: (a) A and B respectively cero cycles treatment at 1350 °C. (b) A and (c) B Dimensional size image of ceramics with melted ashes deposit after four cycles at 1350 respectively, and (d) A and (f) B ash-coupon ensemble respectively after eight cycles of treatment at 1350 °C.

Here, the melted ash formed a microstructure composed by few small grains on the surface, it was also observed the presence of significant microcracks in the layer with a size of several microns. A morphology like scales was identified in the SEM analysis, as observed in Fig. 10(a)–(f), where such vitrified ash was composed by white particles with small aggregates, and some fragments without specific shapes of micro-sized. To elucidate the interaction of raw ash on the 7YSZ ceramics, after thermal treatment at 1350 °C and 8 cycles, a SEM analysis in the cross-section view of the "A" coupon was carried out, as observed in Fig. 11.

In the analysis it was observed a layer of thickness of size of several microns, and with white color on the ceramic surface, which correspond to melted ash, as depicted in Fig. 11(a) and (b). Moreover, last figure shows that this layer was composed by white and gray zones, distribute trough the thickness of the YSZ ceramic substrate, as shown Fig. 11(c).

In Fig. 11(d), it is also observed the formation of microcracks ("holes") of a size around 100 μm with an elongated elliptical shape. The close-up view of both white and gray zones showed that these are constituted of crystal structures embedded by melted ash, as shown in Fig. 11(d). The crystal structures of size of around 15 μm present morphologies likes to tetragonal shapes. The formation of microcracks in the "A" coupon promoted the formation of pores, caused the diffusion of melted ash during thermal treatment through of the thickness of the "A" coupon. An EDAX mapping analysis was also carried out on white and gray zones of the samples in order to confirm the chemical compositions of the corrosion products. Mapping analysis indicated that such zones are composed by Zr, Y and O chemical elements, which correspond to 7YSZ ceramic sample, as observed in Fig. 12(b). The performed EDS mapping also identified rich zones of Si and Al chemical elements constituting an interaction zone, between the melted ash layer and the ceramic substrate, as observed in Fig. 12. It is clearly observed the infiltration of melted ash throughout matrix ceramic, this last result was correlated with above XRD analysis on the presence of ZrO_2 monoclinic phase. Therefore, a depletion of 7YSZ (yttria-stabilized zirconia) caused by the reaction with melted ash is shown, followed by the re-precipitation of both ZrO_2 and Y-depleted monoclinic zirconia. This last finding has also been reported in interactions with synthetic melted ash preparation [28,34–40], nevertheless, according to the authors, the interaction of 7YSZ ceramic and volcanic ash has not been exhaust studied, especially the interaction with nature volcanic ash [4–6,9]. Then, as an approach of the degradation mechanism

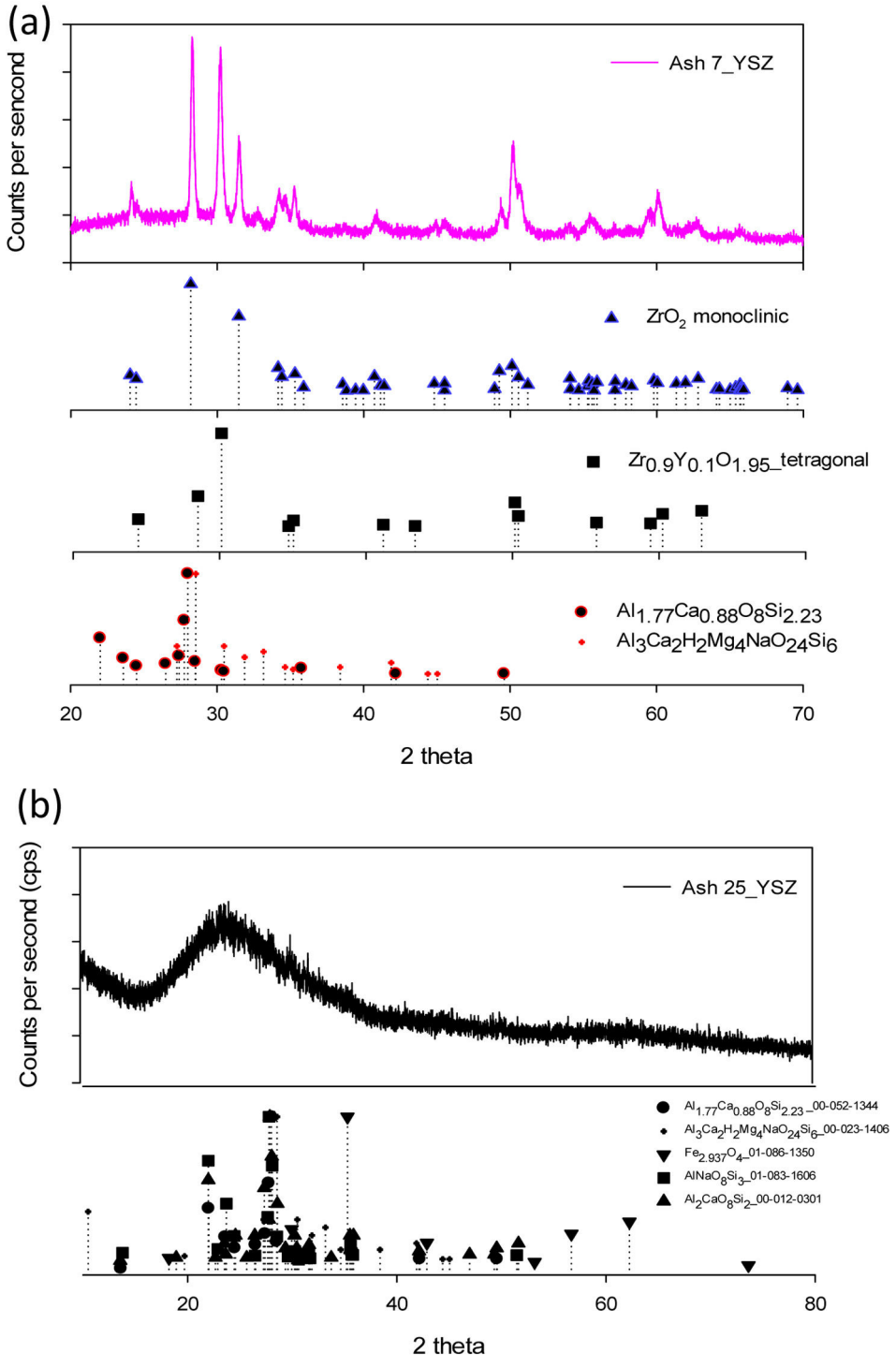

Fig. 8 – XRD analysis of the 7YSZ ceramic after eight cycles of treatment at 1350 °C of temperature with volcanic ash: (a) "A" and (b) "B" coupons respectively.

by melting ash, promoting the onset of cracks of 7YSZ ceramic, is a very important subject of study in the airplane industry in order to give recommendations of their effect in ceramic thermal barrier of jet turbine blades. Fig. 13 shows SEM and EDAX analyses of the "B" coupon in the cross-section view after 8 cycles of thermal treatment at a temperature of 1350 °C. Fig. 13(a) shows the ensemble (melted ash/ceramic coupon), where it can be observed on the top region of the ceramic sample the formation of a layer identified by gray color zone, shown the penetration and the reaction rate of the melted ash, as observed in Fig. 13(b). Nonetheless, it was observed that "B" sample has a lower corrosion potential, compared to "A" ash sample, this can be attributed to the formation of a minor amount of corrosive salts, where it seems to be constituted by

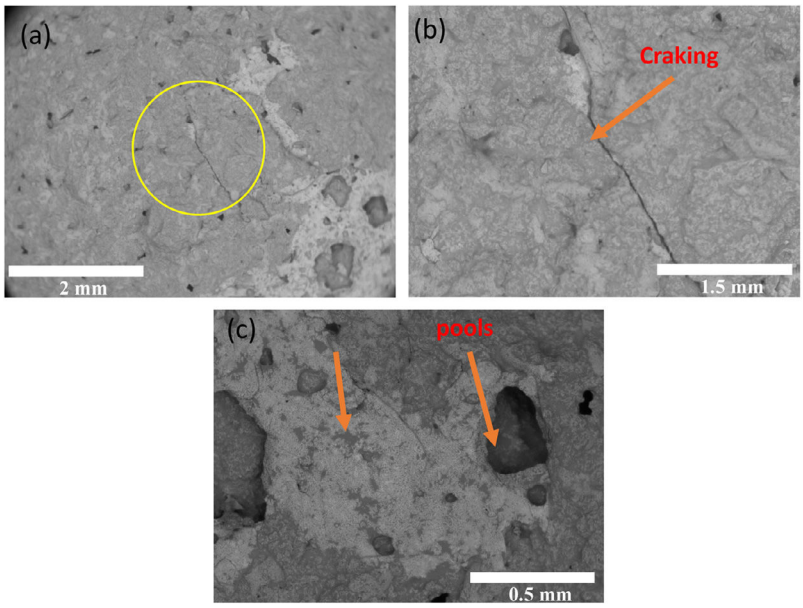

Fig. 9 – SEM analysis of the 7YSZ ceramic after 4 cycles thermal treatment at 1350 °C of temperature with A volcanic ash: (a) melted ash on 7YSZ ceramic, (b) close-up from (a), and (c) porous and cracking of melted ash layer.

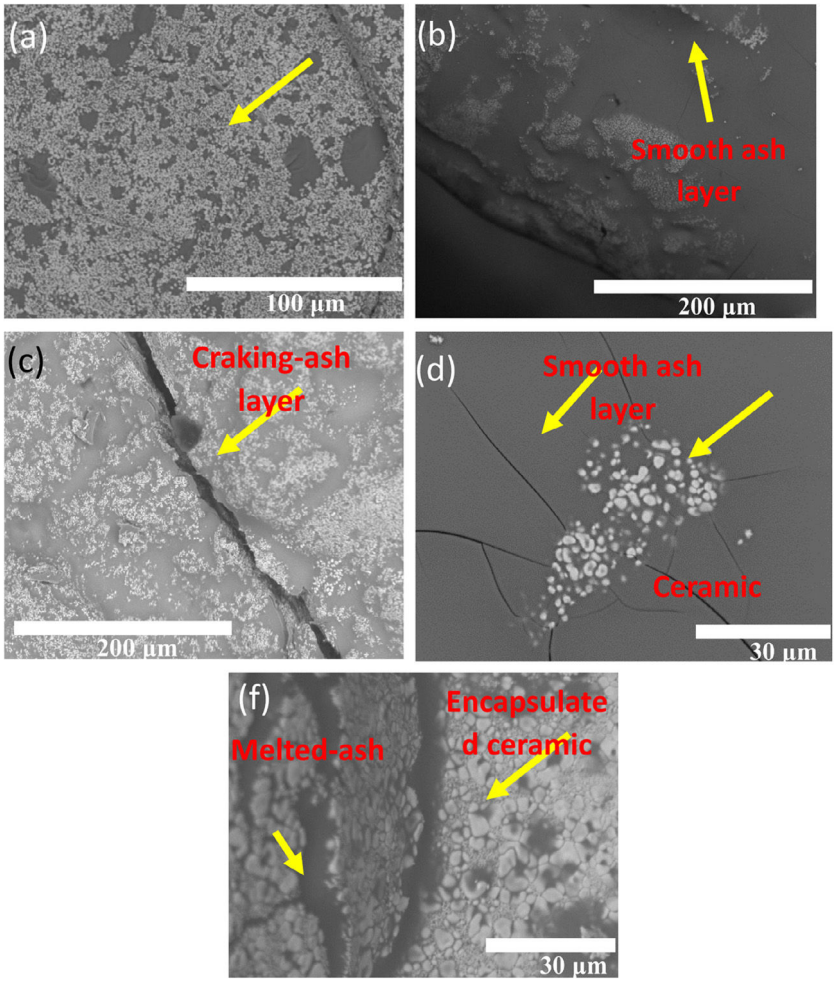

Fig. 10 – SEM analysis of the 7YSZ ceramic after 4 cycles thermal treatment at 1350 °C of temperature with B volcanic ash.

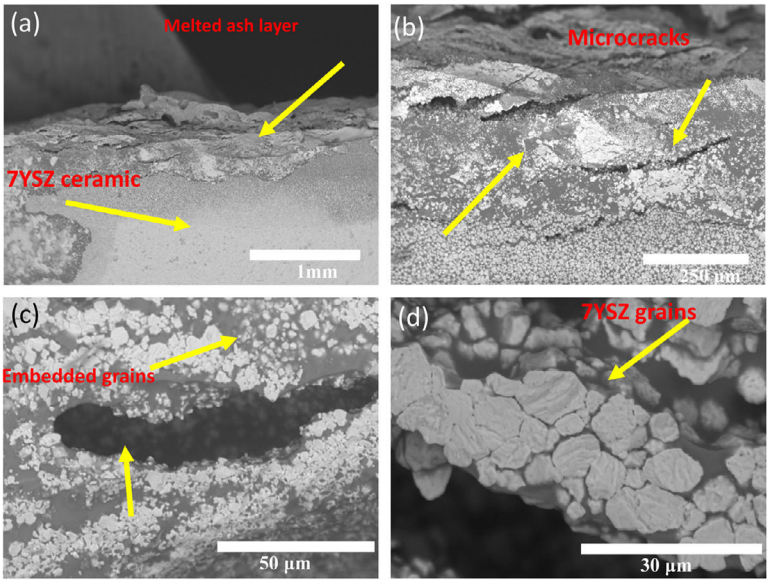

Fig. 11 – SEM analysis in cross-section view of the "A" coupon after 8 cycles thermal treatment at 1350 °C of temperature: (a) melted ash-7YSZ ceramic, (b) close-up from (a), (c) "Hole" formation and (d) close-up view from (c) embedded 7YSZ grains by melted ashes.

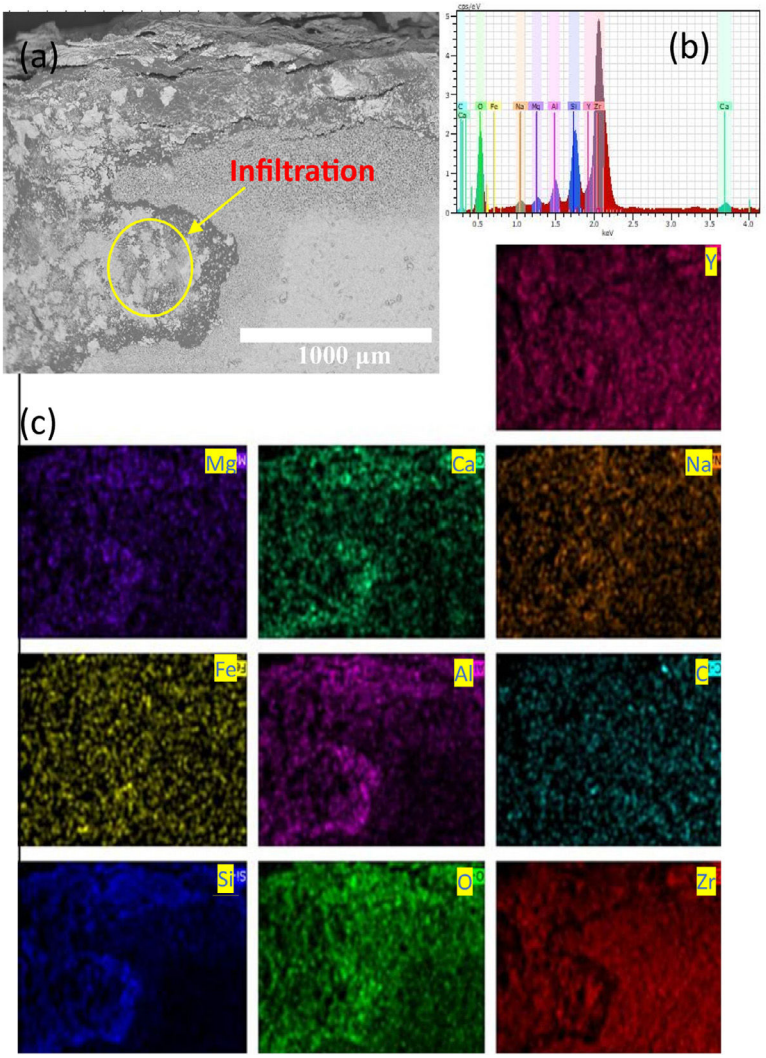

Fig. 12 – (a) SEM analysis in cross-section view of "A" coupon after thermal treatment at 1350 °C of temperature, (b) EDS spectrum analysis and (c) EDS mapping image respectively.

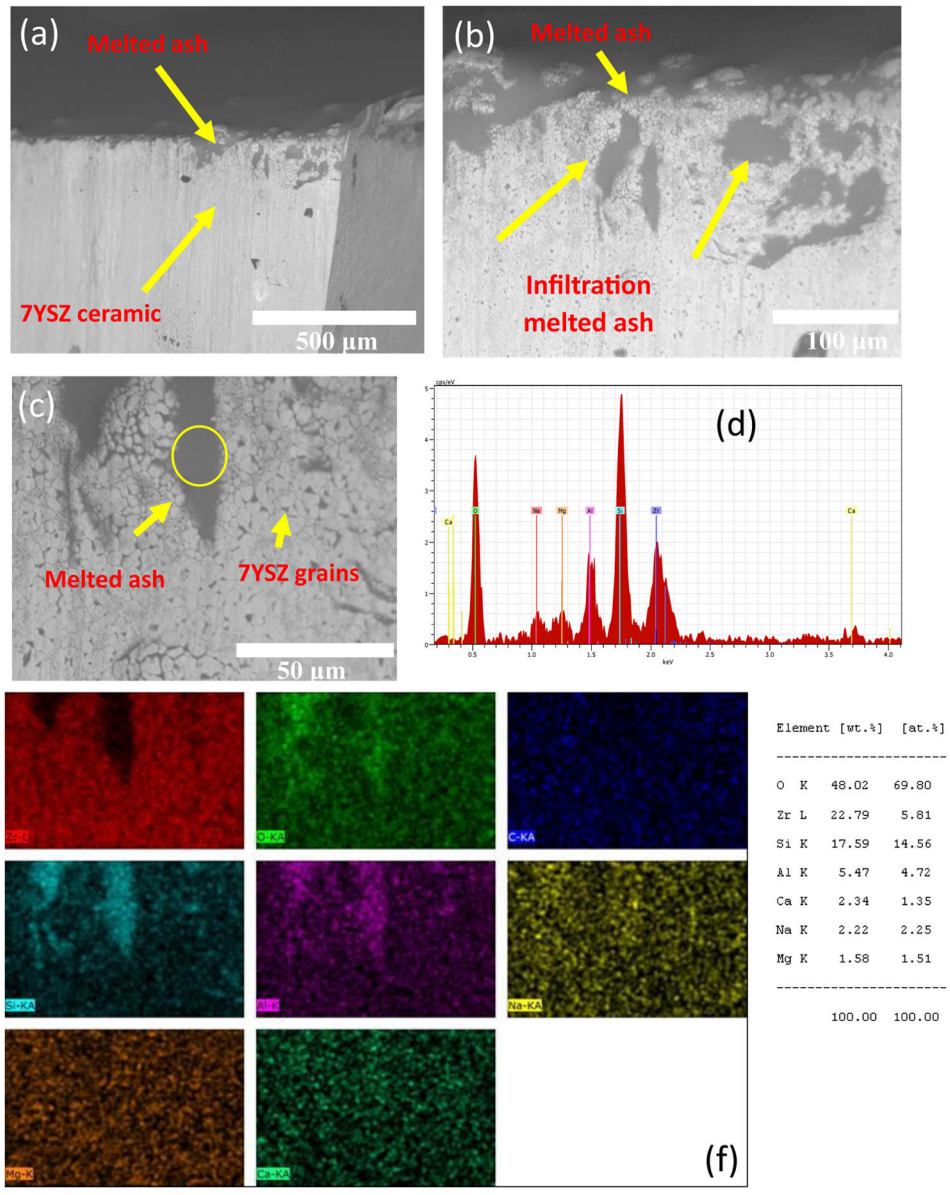

Fig. 13 – SEM analysis in a cross-section view of "B" coupon after thermal treatment at 1350 °C of temperature: (a) micrograph image, (b) close-up from (a), (c) close-up infiltration of melted ash and (d and f) EDS spectrum and mapping analysis respectively.

Si, Na and Ca compounds, wherein the relative concentration distributions of the elements, Zr, Si, O, and Na, are illustrated, as shown in Fig. 13(b) and (c).

It is clear that Al and Si chemical elements were rich in the melted ash layer, as shown by the performed EDS mapping, and a significant Na content was distributed through the thickness of the ceramic, Fig. 13(d). From a close-up view from this zone, it was confirmed the presence of a 7YSZ microstructure in white color, and an amorph layer in gray color, from both white and gray zones showed that they are constituted of crystal structures embedded by melted ash respectively, as observed in Fig. 13(a)–(c). In addition, Al chemical element was detected beneath of the ash layer, which would meaning that a preferential diffusion occurred across of the ceramic coupon, Fig. 13(f).

A detailed BS-SEM qualitative analysis, from both white grains and gray color zones showed the penetration and the reaction rate of the melted ash, as observed in Fig. 14.

The performed BS-SEM analysis collected from the cross-section of "B" sample is presented in Fig. 14(a)–(f). Thus, thermal reaction promoted cracks in the coupons, as observed in Fig. 14, where is showed by the micrograph the infiltration of melted B ash through the YSZ structure, moreover, it is observed the YSZ grains embedded by molten ash, as observed in Fig. 14(b). It worth to note that this cross-section view shows the fracture surface achieved after 8 cycles of thermal treatment at 1350 °C of temperature. In the same sense, the presence of a SiO_2 phase is commonly reported in the hot corrosion of silicon-based ceramics, since the melted sodium silicate Na_2O–xSiO_2 can decompose to silica when x

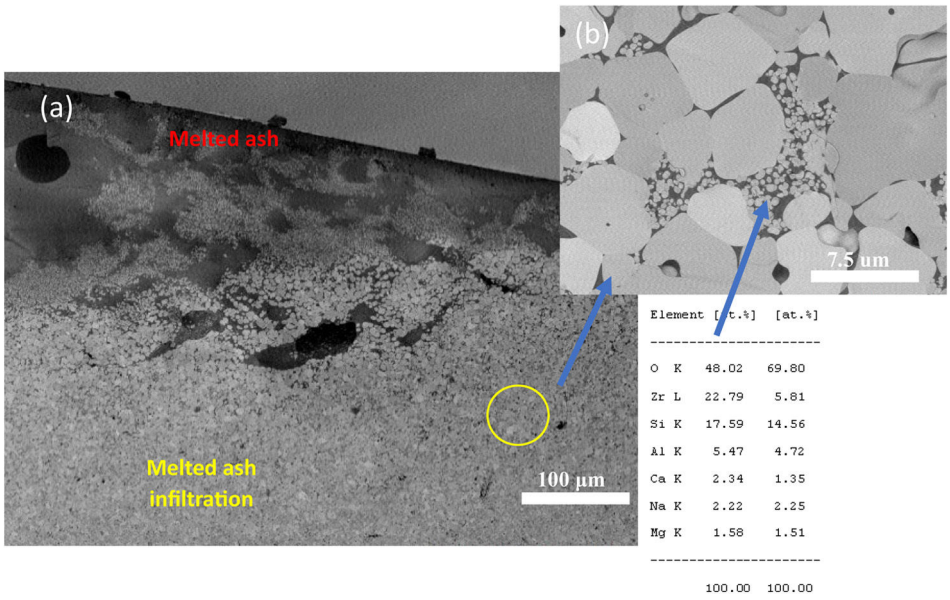

Fig. 14 – SEM analysis in a cross-section view of sintered 7YSZ coupon after treatment at 1350 °C of temperature with B volcanic ash: (a) micrograph and (b) close-up infiltration zone and EDS quantitative analysis respectively.

ration is major of 3.65 [41,42]. Although, the formation of silica beneath the ash layer could protect the ceramic matrix for further hot corrosion [43,44]. In our case, a continuous Si-rich band into matrix ceramic coupon was observed, as shown in Figs. 12 and 13 respectively, and as mentioned above, the XRD results, collected from ceramic samples "A" and "B" with ash deposit, which in turn formed corrosive products, suggested that a vitrified layer existed, and diffused trough the YSZ grains, breaking ceramic bonds, creating continuous microcracks which at some time broke the Y–O bonds during thermal cycle treatment.

Conclusions

The infiltration, at high temperature, of molten ash into sintered 7YSZ coupons was studied in the present work. For the analysis, two different locations – distance from Mexico Volcano were chosen to collect ashes, in order to perform their interaction thermal into 7YSZ ceramic. "A" ash was composed by large particles in the range size from 100 to 400 µm with a fine-grained fraction less than 10 µm, the also showed textural features with roughness surface and morphology granular. In the case of "B" ash, it is composed by a smoother particles fraction ranging from 20 to 100 µm with porous morphology, and a fine-grained fraction less than 10 µm. The analysis showed that after 4 cycles of thermal treatment during 8 h, at high temperature of 1350 °C, the self-melted ash formed a vitrified layer on each sintered 7YSZ ceramic coupon. Although, the presence of smalls microcracks on the ceramic surface, the appearance of slight damage of both "A" and "B" coupon was noted. Based on the last early results, it was decided that both "A" and "B" coupons were thermal treatment, at the temperature of 1350 °C up until appearance of failure in the coupon. The analysis showed that after 8 cycles of heat during 8 h, at the designed temperature, both coupons presented significant failure. Afterward, a cross-section analysis of coupons showed the formation of crystals with morphology like to salt shapes, localized underneath the vitrificated ash layer on the ceramic surface. These crystals were rich in content of Si and Al elements, with higher Na, Ca, and K constituent, which constituted a vitrified ash layer on the ceramic coupon. In the "A" coupon case, it was promoted the of cracking and crack growth, with a size of about 10 µm into 7YSZ matrix, caused by the infiltration and reaction of $Al_{1.77}Ca_{0.88}O_8Si_{2.23}$ and $Al_3Ca_2H_2Mg_4NaO_{24}Si_6$ minerals compounds, which shaped the molten ash. Moreover, the XRD results showed clearly a transition of ZrO_2 tetragonal to ZrO_2 monoclinic, caused by Y depletion from 7YSZ ceramic matrix. In the "B" coupon case, the 7YSZ ceramic degradation was delayed by the develop of an amorph thick ash layer, which predominately postpones the reaction of O^{2-} and Si^{2+} with zirconia crystals, and damage and rupture were finally reached for both "A" and "B" coupons.

Acknowledgments

The authors acknowledge to: Comisión de Fomento a las Actividades Académicas, Estimulo al desempeño de los Investigadores; Sistema Nacional de Investigadores, Consejo Nacional de Humanidades, Ciencia y Tecnología (CONAHCYT) México; and Rubén Cuamatzi-Meléndez to México Postdoctoral Stays 2022 (3) No. I1200/320/2022 for the provided support. Special acknowledgment to Ricardo Escalona G. by coupons preparation.

REFERENCES

[1] S. Anandh Jesuraj, P. Kuppusami, A.M. Kamalan Kirubaharan, M. Rajasekaramoorthy, Advanced Ceramic

Coatings for Emerging Applications, 1st edition, Elsevier, 2023, pp. 151–183, ISBN: 9780323996259.
[2] G. Ram, M. Amir, K. Saeid, A.N. Tuan, B. Ajit, Advanced Ceramic Coatings for Emerging Applications, 1st edition, Elsevier, 2023, http://dx.doi.org/10.1016/C2021-0-01944-1.
[3] L. Lirong, C. Ying, Z. Xiaofeng, Thermal Barrier Coatings. Strategies for Improving the Lifetime of Air Plasma Sprayed Thermal Barrier Coatings, 2nd edition, Elsevier, 2023, pp. 325–360, http://dx.doi.org/10.1016/B978-0-12-819027-2.00007-9.
[4] S. Wenjia, S. Uwe, G. Hongbo, B.D. Donald, Thermal Barrier Coatings. Volcanic Ash Hazards to Aviation Safety, 2nd edition, Elsevier, 2023, pp. 293–324, http://dx.doi.org/10.1016/B978-0-12-819027-2.00009-2.
[5] J. Xia, L. Zhang, Y. Matsushita, R.T. Wu, Evolution of the microstructure and mechanisms of performance degradation in EB-PVD YSZ thermal barrier coatings corroded by volcanic ash at 1150 °C, Corros. Sci. 208 (2022) 110626, http://dx.doi.org/10.1016/j.corsci.2022.110626.
[6] A.L. Martin-Del Pozzo, T. González-Morán, R. Espinasa-Pereña, M.A. Butron, M. Reyes, Characterization of the recent ash emissions at Popocatepetl Volcano, Mexico, J. Volcanol. Geotherm. Res. 170 (2008) 61–75, http://dx.doi.org/10.1016/j.jvolgeores.2007.09.004.
[7] M. Prabhakar, P. Travis, S. Yongho, Degradation of thermal barrier coatings by molten CMAS ($CaO–MgO–Al_2O_3–SiO_2$) deposits, in: AIAA, 2009, pp. 1–10, http://dx.doi.org/10.2514/6.2009-1433.
[8] A. Játiva, E. Ruales, M. Etxeberria, Volcanic ash as a sustainable binder material: an extensive review, Materials 14 (2021) 1302, http://dx.doi.org/10.3390/ma14051302.
[9] L. Ma, W. Song, Z. Guo, X. Zou, D.B. Dingwell, Dynamic melting behavior of volcanic ash subjected to thermal shock relevant to aviation hazards, J. Volcanol. Geotherm. Res. 429 (2022) 107597, http://dx.doi.org/10.1016/j.jvolgeores.2022.107597.
[10] S. Alraddadi, Effects of calcination on structural properties and surface morphology of black volcanic ash, J. Phys. Commun. 4 (2020) 105002, http://dx.doi.org/10.1088/2399-6528/abbcdc.
[11] S. Alraddadi, A. Saeed, H. Assaedi, Effect of thermal treatment on the structural, electrical, and dielectric properties of volcanic scoria, J Mater. Sci.: Mater. Electron. 31 (2020) 11688–11699, http://dx.doi.org/10.1007/s10854-020-03720-0.
[12] Y. Wu, D. He, $NdYbZr_2O_7$ thermal barrier coating resistant to degradation by volcanic ash and CMAS, Corros. Sci. 209 (2022) 110795, http://dx.doi.org/10.1016/j.corsci.2022.110795.
[13] K. Ramachandran, B. Chaffey, C. Zuccarini, J.C. Bear, D.D. Jayaseelan, Experimental and mathematical modelling of corrosion behaviour of CMAS coated oxide/oxide CMCs, Ceram. Int. 49 (2023) 4213–4221, http://dx.doi.org/10.1016/j.ceramint.2022.09.294.
[14] M.D. Thouless, Cracking and delamination of coatings, J. Vac. Sci. Technol. A: Vac. Surf. Films 9 (1991) 2510–2515, http://dx.doi.org/10.1116/1.577265.
[15] G. Mehboob, T. Xu, G.R. Li, S. Hussain, G. Mehboob, A. Tahir, Strain-induced cracking behavior of coating/substrate systems and strain tolerant design for thick coatings, Coatings 10 (2020) 1066, http://dx.doi.org/10.3390/coatings10111066.
[16] S. Chi, Y.L. Chung, Cracking in coating–substrate composites with multi-layered and FGM coatings, Eng. Fract. Mech. 70 (2003) 1227–1243, http://dx.doi.org/10.1016/S0013-7944(02)00114-5.
[17] J. Feng, Y. Qin, T.W. Liskiewicz, B.D. Beake, S. Wang, Crack propagation of a thin hard coating under cyclic loading: irreversible cohesive zone model, Surf. Coat. Technol. 426 (2021) 127776, http://dx.doi.org/10.1016/j.surfcoat.2021.127776.
[18] R. Wellman, G. Whitman, J.R. Nicholls, CMAS corrosion of EB PVD TBCs: identifying the minimum level to initiate damage, Int. J. Refract. Metals Hard. Mater. 28 (2010) 124–132, http://dx.doi.org/10.1016/j.ijrmhm.2009.07.005.
[19] M.H. Vidal-Setif, N. Chellah, C. Rio, C. Sanchez, O. Lavigne, Calcium–magnesium–alumino-silicate (CMAS) degradation of EB-PVD thermal barrier coatings: characterization of CMAS damage on ex-service high pressure blade TBCs, Surf. Coat. Technol. 208 (2012) 39–45, http://dx.doi.org/10.1016/j.surfcoat.2012.07.074.
[20] Y. Hayashi, S. Yamagishi, M. Okazaki, Damage progression of thermal barrier coatings by CMAS, J. Soc. Mater. Sci. Jpn. 64 (2015) 134–139, http://dx.doi.org/10.2472/jsms.64.134.
[21] L. Li, N. Hitchman, J. Knapp, Failure of thermal barrier coatings subjected to CMAS attack, J. Therm. Spray Technol. 19 (2010) 148–155, http://dx.doi.org/10.31399/asm.cp.itsc2009p0077.
[22] V.L. Wiesner, N.P. Bansal, Crystallization kinetics of calcium–magnesium aluminosilicate (CMAS) glass, Surf. Coat. Technol. 259 (2014) 608–615, http://dx.doi.org/10.1016/j.surfcoat.2014.10.023.
[23] S. Liu, Q. Liu, X. Hu, J. Guo, W. Zhu, F. Zhang, J. Xia, CMAS corrosion resistance behavior and mechanism of $Hf_6Ta_2O_{17}$ ceramic as potential material for thermal barrier coatings, Coatings 13 (2023) 404, http://dx.doi.org/10.3390/coatings13020404.
[24] X. Zhang, H. Xin, L. Guo, Crystallization behavior of calcium–magnesium–alumina–silicate coupled with $NaCl/Na_2SO_4$, Corros. Commun. 10 (2023) 1–9, http://dx.doi.org/10.1016/j.corcom.2022.08.003.
[25] E. Serrano Pérez, H. Martinez Gutierrez, K.J. Martinez Gonzalez, E. Marín Moares, F. Juárez López, Densification and microstructure of spark plasma sintered 7YSZ–Gd_2O_3 ceramic nano-composites, J. Asian Ceram. Soc. 5 (2017) 266–275, http://dx.doi.org/10.1016/j.jascer.2017.05.004.
[26] C. Holgatea, G.G.E. Seward, A.R. Ericks, D.L. Poerschke, C.G. Levi, Dissolution and diffusion kinetics of yttria-stabilized zirconia into molten silicates, J. Eur. Ceram. Soc. 41 (2020) 2–28, http://dx.doi.org/10.1016/j.jeurceramsoc.2020.10.056.
[27] F.M. Pitek, C.G. Levi, Opportunities for TBCs in the $ZrO_2–YO_{1.5}–TaO_{2.5}$ system, Surf. Coat. Technol. 201 (2007) 6044–6050, http://dx.doi.org/10.1016/j.surfcoat.2006.11.011.
[28] M.V. Mendoza, R.C. Alvarez, F. Juárez López, Combustion flame spray of 7YSZ powders followed by corrosion in molten salts of the coating, J. Asian Ceram. Soc. 9 (2021) 617–628, http://dx.doi.org/10.1080/21870764.2021.1905266.
[29] J.M. Brown, R.J. Angel, N.L. Ross, Elasticity of plagioclase feldspars, J. Geophys. Res. Solid Earth 121 (2016) 663–675, http://dx.doi.org/10.1002/2015JB012736.
[30] M. Mookherjee, D. Mainprice, K. Maheshwari, O. Heinonen, D. Patel, A. Hariharan, Pressure induced elastic softening in framework aluminosilicate-albite ($NaAlSi_3O_8$), Sci. Rep. 6 (2016) 34815, http://dx.doi.org/10.1038/srep34815.
[31] F. Locati, S. Marfil, E. Baldo, P. Maiza, Na_2O, K_2O, SiO_2 and Al_2O_3 release from potassic and calcic–sodic feldspars into alkaline solutions, Cem. Concr. Res. 40 (2010) 1189–1196, http://dx.doi.org/10.1016/j.cemconres.2010.04.005.
[32] C.F. Nalle, R. Wahid, I.O. Wulandari, A. Sabarudin, Synthesis and characterization of magnetic Fe_3O_4 nanoparticles using oleic acid as stabilizing agent, Rasayan J. Chem. 12 (2019) 14–21, http://dx.doi.org/10.31788/RJC.2019.1214082.
[33] G. Kletetschka, P.J. Wasilewski, P.T. Taylor, The role of hematite–ilmenite solid solution in the production of magnetic anomalies in ground- and satellite-based data, Tectonophysics 347 (2002) 167–177, http://dx.doi.org/10.1016/S0040-1951(01)00243-8.

[34] U. Schulz, W. Braue, Degradation of $La_2Zr_2O_7$ and other novel EB-PVD thermal barrier coatings by CMAS ($CaO–MgO–Al_2O_3–SiO_2$) and volcanic ash deposits, Surf. Coat. Technol. 235 (2013) 165–173, http://dx.doi.org/10.1016/j.surfcoat.2013.07.029.

[35] M.H. Vidal-Sétif, C. Rio, D. Boivin, O. Lavigne, Microstructural characterization of the interaction between 8YPSZ (EB-PVD) thermal barrier coatings and a synthetic CAS, Surf. Coat. Technol. 239 (2014) 41–48, http://dx.doi.org/10.1016/j.surfcoat.2013.11.014.

[36] P. Mohan, B. Yuan, T. Patterson, V. Desai, Y.H. Sohn, Degradation of yttria stabilized zirconia thermal barrier coatings by molten CMAS ($CaO–MgO–Al_2O_3–SiO_2$) deposits, Mater. Sci. Forum 595 (2008) 207–212, http://dx.doi.org/10.4028/www.scientific.net/MSF.595-598.207.

[37] S. Morelli, V. Testa, G. Bolelli, O. Ligabue, E. Molinari, N. Antolotti, L. Lusvarghi, CMAS corrosion of 7YSZ thermal barrier coatings obtained by different thermal spray processes, J. Eur. Ceram. Soc. 40 (12) (2020) 4084–4100.

[38] L. Zou, M. Gao, N. Xu, J. Zhang, X. Chang, CMAS corrosion behavior of nanostructured 7YSZ and Gd-Yb-Y-stabilized zirconia coatings, Coatings 13 (9) (2023) 1623.

[39] P. Zhang, X. Zhang, F. Li, Z. Zhang, Y. Wang, H. Li, L. Ren, M. Liu, Hot corrosion behavior of 7YSZ thermal barrier coatings modified by laser remelting and Al deposition, J. Therm. Spray Technol. 28 (6) (2019) 1225–1238.

[40] P. Bajpai, A. Das, P. Bhattacharya, S. Madayi, K. Kulkarni, S. Omar, Hot corrosion of stabilized zirconia thermal barrier coatings and the role of Mg inhibitor, J. Am. Ceram. Soc. 98 (8) (2015) 2655–2661.

[41] Z. Sun, M. Li, Z. Li, Y. Zhou, Hot corrosion of γ-$Y_2Si_2O_7$ in strongly basic Na_2CO_3 molten salt environment, J. Eur. Ceram. Soc. 28 (2008) 259–265, http://dx.doi.org/10.1016/j.jeurceramsoc.2007.05.011.

[42] Z. Sun, M. Li, Y. Zhou, Recent progress on synthesis, multi-scale structure, and properties of Y–Si–O oxides, Int. Mater. Rev. 59 (2014) 357–383, http://dx.doi.org/10.1179/1743280414Y.0000000033.

[43] R. Rajkumar, C. Vedhi, A study of corrosion protection efficiency of silica nanoparticles acrylic coated on mild steel electrode, Vacuum 161 (2019) 1–4, http://dx.doi.org/10.1016/j.vacuum.2018.12.005.

[44] J. Gąsiorek, A. Szczurek, B. Babiarczuk, J. Kaleta, W. Jones, J. Krzak, Functionalizable sol–gel silica coatings for corrosion mitigation, Materials 11 (2018) 197, http://dx.doi.org/10.3390/ma11020197.